UCRL-ID--105130

DE91 002574

Geometric Effects in Tomographic Reconstruction

Freddie L. Barnes, Stephen G. Azevedo, Harry E. Martz, Jr.,
G. Patrick Roberson, Daniel J. Schneberk, and Michael F. Skeate

Lawrence Livermore National Laboratory
Nondestructive Evaluation Section
P. O. Box 333, L-333
Livermore, CA 94550

ABSTRACT

In x-ray and ion-beam computerized tomography, there are a number of reconstruction effects, manifested as artifacts, that can be attributed to the geometry of the experimental setup and of the object being scanned. In this work, we will examine four geometric effects that are common to first- and third-generation (parallel beam, 180 degree) computerized tomography (CT) scanners and suggest solutions for each problem. The geometric effects focused on in this paper are: "X-pattern" artifacts (believed to be caused by several errors), edge-generated ringing artifacts (due to improper choice of the reconstruction filter and cutoff frequency), circular-ring artifacts (caused by employing uncalibrated detectors), and tuning-fork artifacts (generated by an incorrectly specified center-of-rotation). Examples of all four effects are presented. The X-pattern and edge-generated ringing artifacts are presented with actual experimental data introducing the artifact. Given the source of the artifact, we present simulated data designed to replicate the artifact. Finally, we suggest ways to reduce or completely remove these artifacts. The circular-ring and tuning-fork artifacts are introduced with actual experimental data as well, while digital signal processing solutions are employed to remove the artifacts from the data.

I. INTRODUCTION

Artifacts in CT images are due to many factors [MAR89, SCH89, SCH90]. A partial list is as follows:

- Noise due to photon counting, photon scattering, electronic noise, beam-hardening, etc.,
- Insufficient data as in the limited-view or limited-angle situations,
- Reconstruction algorithm effects,
- Geometric effects of object shape (*e.g.*, large aspect ratio) and data acquisition.

Each of these factors should be considered in the experimental design and data analysis, and deserve considerable study. However, this report focuses only on a few types of common geometric effects that arise in experimental practice: (1) "X-pattern" artifacts within square objects are believed to be caused by several errors, (2) edge-generated ringing artifacts are due to reconstruction filter characteristics, (3) circular-ring artifacts are due to uncalibrated detectors, and (4) tuning-fork artifacts are resulting from an incorrectly specified center of rotation.

We can achieve improved CT reconstructions by paying careful attention to all sources of potential error in CT scanning systems [MAR89] and the reconstruction codes [SCH90]. The four geometric effects specifically described above have their own characteristic error signatures that can be identified, and software solutions can be applied to improve the data quality.

For all reconstructions discussed in this work, we assume:

- Uniformly-spaced detectors along a straight line in each projection,
- Parallel-beam source illumination (or, for a fan-beam, the ability to re-bin the data into this form),
- Use of the filtered backprojection (FBP) algorithm [HER80] with linear interpolation between the rays for the reconstruction process.

II. BACKGROUND

A) The forward CT problem

In CT, the goal is to extract information about the interior of an object by constructing a cross-sectional image (or 2D slice plane) of the object from projection data. The projected rays are the measurements of the integrated values of an object parameter along straight

lines through the object. For an x-ray scanner [MAR88], the object parameter is the linear attenuation coefficient per unit volume; then the line integral represents the total attenuation of the x-ray beam as it travels in a straight line through the object. For a proton-energy-loss (PEL) CT scanner, the object parameter of interest is the total number of electrons per unit volume. The measured proton energy loss, determined from the residual energy of the transmitted protons, are converted to electrons per unit area (a line-integral of electrons illuminated by the beam) before image reconstruction.[PON89, ANT89].

A projection is formed by combining a set of line integrals. Computationally the simplest type of projection to work with is the parallel projection. This is the case where each line integral in a projection represents a collection of parallel rays passing through the object at a fixed angle. In an actual experimental set-up, a parallel projection could be measured by moving a single source and a single detector along parallel lines on opposite sides of an object, or by translating the object between a fixed source and detector. This is known as a first generation CT scanning arrangement.

A second type of projection, known as a fan-beam projection, uses a single point source placed in a fixed position relative to a line, or array, of detectors. The resulting projection is called a fan-beam projection because the line integrals are measured along a collection of rays that form a fan for each angle of rotation. Since fan-beam projection data can be rearranged or "rebinned" into parallel projections, we will concern ourselves with parallel projection data only.

Next, we develop a mathematical model that expresses the attenuation coefficient in terms of the measured intensity. Consider that we have a single monoenergetic beam of x-ray photons (less than 1.022 MeV to avoid pair production) propagating through some material. The beam attenuation is due to either photons completely absorbed by the material (photoelectric absorption), or the scattering of photons from the original direction of travel.[BAR81] Consider an incremental thickness of this material in which N_0 monoenergetic photons are incident upon it at some unspecified time. Due to attenuation, somewhat less than N_0 photons emerge from the other side. If we combine the photon loss rate and the Compton effects into one linear attenuation parameter, μ, then the number of photons as a function of position within the slab can be modeled as

$$N(l) = N_0 \exp(-\mu l), \qquad (1)$$

where μ is assumed constant over the slab and l is the distance through the slab. For non-uniform objects, where μ changes with material, we can assume that the effects of small regions on the total beam attenuation can be integrated. Let us represent the linear attenuation coefficient at each small region in a single slice plane by $\mu(x,y)$, where x and y are spatial Cartesian coordinates. Then using $N_0(L)$ to be the number of incident photons along a beam path L, the number of exiting photons, $N(L)$, will be

$$N(L) = N_0(L) \exp\left[- \int_L \mu(x,y)\, du \right], \tag{2}$$

where u is the integration distance along L. By exploiting the linear relationship between the number of photons and intensity (number of photons per unit time-area), the above expression can be written in terms of beam intensity, or

$$I(L) = I_0(L) \exp\left[- \int_L \mu(x,y)\, du \right], \tag{3}$$

where I_0 is the measured incident intensity and I is the transmitted intensity. If we further define $g(s,\theta)$ as the linear attenuation line-integral through space along a line defined by the polar coordinates s and θ (which represent the point of closest approach of the line from the origin), then

$$g(s,\theta) = \int_L \mu(x,y)\, du , \tag{4}$$

where s is in the range $(-\infty,+\infty)$ and θ is in the range $(0,\pi)$. Therefore, we have

$$g(s,\theta) = \ln\left[\frac{I_0(s,\theta)}{I(s,\theta)} \right]. \tag{5}$$

The above relationship expresses the attenuation coefficient line integrals in terms of measured intensity values. The $g(s,\theta)$ values are the ones to be reconstructed (see next section). Our scanners measure I_0 first, without the object in the beam-path, then they take multiple measurements of $I(s,\theta)$ at various s and θ. After calibration and preprocessing, the line integrals are computed as in Equation 5. The incident intensity, I_0, is shown here to be a constant, but it too can vary over the field.

In PEL computerized tomography, line-integral values must also be derived from the actual measurements. For an explanation of the determination of I and I_0 (in this case the intensity is a measure of electrons per unit area) from PEL data, see [ANT89]. It is possible that errors in the measurement or determination of the incident intensity, I_0, can occur in both x-ray and PEL experiments. We will examine the effects of this error in the section on X-pattern artifacts observed in square objects.

B) The inverse CT problem

From the line integral measurements, $g(s,\theta)$, we must use a computer algorithm to reconstruct the slice plane into a 2D image. There are several ways to accomplish this, but the algorithm used in many applications of tomography is the filtered backprojection algorithm. It has been shown to be reasonably accurate and amenable to fast implementation when presented with complete projection data [JAI89, AZE88].

The basis of the FBP algorithm is the Fourier Slice Theorem. The Fourier Slice Theorem shows the equivalence of the one-dimensional Fourier transform of a projection to the two-dimensional Fourier transform of the object along a single radial slice. Given the Fourier transforms of projections from enough angles, a complete estimate of the two-dimensional transform could be assembled and then inverted to arrive at an image estimate. Conceptually, this approach is straight forward, but impractical because the interpolation required before inversion is very sensitive to errors. Instead, the analytic derivation of FBP stems directly from the Fourier Slice theorem [JAI89], and we find it to be more commonly used. All the analyses in this report use the FBP algorithm.

The FBP algorithm for parallel projections consists of performing the following steps for each projection angle:

- Measure the projection and convert to the line integrals $g(s,\theta)$,
- Compute the one-dimensional Fourier transform of each projection,
- Apply the appropriate weighted filter function,
- Inverse Fourier transform the filtered projection,
- Sum the filtered projections over the image plane along the integration lines (this is the backprojection operation).

The image starts at zero and the result of backprojecting all of the filtered projections produces the final reconstructed image.

III. RESULTS AND DISCUSSION

In this section, we will describe each geometric effect in turn and suggest solutions to them. Where possible, alternate sources of more detailed information will be given.

A) "X-pattern" artifact observed in square objects

Reconstructed images of homogeneous square objects using x-ray and PEL CT data sometimes result in an X pattern within the reconstructed image. This is observed in the PEL images shown in Figure 1, and could be due to any or all of the following: incorrectly computed electron areal density value, the partial volume effect, Coulomb repulsion causing spreading of the beam, effective "beam softening" (an effective shift of the proton beam to lower energy as it traverses the object most noticeable along diagonals of a square or rectangular object), or some other unmodeled effect in the preprocessing. There was also some question as to whether the X pattern is a result of the reconstruction algorithm. In this work, we test only two of the above theories — the reconstruction algorithm and a simulated incorrect electron areal density or x-ray intensity values — and suggest further studies to isolate the actual cause from the groundwork laid here.

The first task is to verify the reconstruction algorithm by showing that if the data represents perfect (simulated) line-integrals through a square object, the reconstruction algorithm is not responsible for the X-pattern artifact. We begin by simulating a two dimensional square object as shown in Figure 2(a). The object consists of a 64 by 64 pixel image with a centered 32 by 32 square of attenuation value 1. The projections for a first generation scanning configuration were simulated with the software package CTSIM [AZE90]. This package computes the noiseless line integrals, $g(s,\theta)$, through the object of interest. The reconstruction from these simulated projections, shown in Figure 2(a), reveals a uniform square image as expected. This proves that, given correct projections from a square object, the reconstruction algorithm produces the correct image. Therefore, for the PEL data, the reconstruction algorithm is *not* responsible for the X-pattern artifact, and fault must lie with one or a combination of the effects mentioned above.

Secondly, let us examine the effects of incorrectly measuring or computing the incident intensity value. We investigate the effect of the multiplicative error in I_0 with no error in the $I(s,\theta)$ measurements. To see these effects mathematically, let us multiply I_0 from Equation 5 by a constant, C_1:

$$\begin{aligned} g'(s,\theta) &= \ln\left[\frac{I_0(s,\theta) * C_1}{I(s,\theta)}\right] \\ &= \ln\left[\frac{I_0(s,\theta)}{I(s,\theta)}\right] + \ln[C_1] \\ g'(s,\theta) &= g(s,\theta) + \ln[C_1] \,. \end{aligned} \tag{6}$$

A multiplicative error in I_0 leads to an offset or bias in the line integrals. If $C_1>1$, the line integrals are biased by adding the natural logarithm of the constant value. If $C_1<1$, the line integrals are biased by subtracting the natural logarithm of the constant value.

We have generated data sets with different values of C_1 and reconstructed them (Figures 2 and 3). This was accomplished by simulating the projections through the object, subtracting or adding a bias to the projections, setting negative values to zero, and reconstructing the biased projections. In the first case the projections were reduced by an offset that was 50%, 30%, and 10% of their maximum value (illustrated in Figures 2(b), (c), and (d) respectively). These images all display reconstruction artifacts, the most pronounced being the 50% image. The accompanying one-dimensional plots in Figures 2(e) and (f) display the respective horizontal and diagonal line-outs from Figure 2(a), (b), (c), and (d).

In the other case, projections were increased by an offset that was 50%, 30%, and 10% over their maximum value and are illustrated in Figures 3(b), (c), and (d) respectively. Again, the accompanying one-dimensional plots (Figures 3(e) and (f)) display the respective horizontal and diagonal line-outs from Figure 3(a), (b), (c), and (d).

This study indicates the importance of correctly measuring or calculating the incident intensity. Also, it has been verified that the image reconstruction algorithm does not produce the X-pattern artifact. Finally, although an incorrect source intensity produces artifacts, these artifacts do not closely match the X-patterns in Figure 1. However, Figure 2(b) does display somewhat of an X pattern and thus the data in Figure 1 may be partly due to an inaccurate measurement of I_0. Furthermore, we conclude that the X pattern in Figure

1 may also be due to other preprocessing steps that form the line-integrals. Likely candidates are the partial volume effect due to the finite width of the proton beam and the proton beam softening. Further studies are being conducted to investigate these hypotheses.

B) Edge-generated ringing artifacts

In this section, the effects of filter type and cutoff specification are studied. As previously discussed [SCH89], the filtering operation is an essential element in the filtered backprojection algorithm. The choice of an incorrect filter or Gibb's phenomenon (caused by a sharp cutoff in the filter window) can create artifacts in the reconstructed image. This problem manifests itself as oscillatory intensity variations near the edges of sharp objects and sometimes throughout the reconstructed image. Figure 4 shows examples of edge-generated artifacts in the reconstruction of circular objects from real experimental x-ray data. The actual projection data were reconstructed with a ramp filter [SCH89] and normalized cutoff frequencies of 0.15, 0.25, and 0.35 times the fold-over frequency, as shown in Figure 4(a), (b) and (c) respectively.

For ease in the comparison of various filters and cutoff values, in the following discussion we use only simulated data. The projections for a perfect circle and square are calculated. We then apply our FBP algorithm with the ramp and Butterworth filters at several different cutoff frequencies. The reconstructions are then compared.

The first experiment utilizes an object consisting of a 64 by 64 pixel image with an included circle of 16 pixel radius, with unity attenuation value throughout the circle. The projections are generated and the FBP algorithm is applied with the ramp and Butterworth filters for cutoffs of 0.1, 0.3, and 0.5 (as shown in Figures 5, 6 and 7). The reconstructions that use the ramp filter show more of the ringing artifact (see Figure 5(b), (c), and (d)). The most pronounced ringing is present in the ramp filter with a 0.1 normalized cutoff frequency. This can be attributed to the sharp cutoff in the frequency region where the data contains significant energy. This is very similar to convolving the data with an ideal low-pass filter (which has a sinc function as its frequency response) introducing the Gibb's phenomena. The Butterworth filter, on the other hand, produces significantly less ringing but the edges tend not to be as clear. This is due to the fact that Butterworth low-pass filters are characterized by the property that the magnitude characteristic is maximally flat at the frequency origin, and the slope of the roll-off is finite (*i.e.*, more graceful in its descent)

[RAB75]. The lower frequencies reconstruct quite well, while the higher frequency information is filtered out by the filter roll-off and consequently is unavailable for reconstruction. (Sharp edges require higher frequencies in their frequency representation.)

In the second set of experiments, the simulated circular object was replaced with a square object. The second object consisted of a 64 by 64 pixel image with an included 32 by 32 square at the center-of-rotation with an attenuation value of 1. Projections are generated and the FBP algorithm is applied with the ramp and Butterworth filters with parameters identical to those of the first set. As in the first set of experiments, the most pronounced ringing was with the ramp filter and a cutoff frequency of 0.1. These results are shown in Figures 8, 9, and 10.

This study suggests that the Butterworth filter reduces the ringing artifact while the ramp filter seems to produce sharper edges at the same cutoff. It is important to determine the "best" filter based on noise, edge sharpness and edge ringing, and select that combination of parameters which insure the reconstructed data to be of acceptable quality for the intended application [SCH89].

C) Circular-ring artifacts

There are many applications that use a third-generation scanning geometry [HER80]. An inherent problem with this class of scanner becomes apparent with uncalibrated or imbalanced detectors [SCH89] within the detector array. Gain or offset imbalances from detector to detector in linear- or area-array detector systems produces vertical lines in the sinogram (set of projections). Consequently, concentric rings are introduced in the reconstructed image. The prevalence of this systematic error in several of our scanners motivates our interest in this study.

The multiple detectors are calibrated and software solutions are applied in an effort to correct for gain and offset imbalances in our third-generation CT scanners [MAR89], but it often does not completely eliminate these imbalances early in the preprocessing phase. Thus, we perform further corrections using techniques which will minimize this artifact. The approach we use, suggested by Kowalski [KOW78], essentially consists of ensemble averaging the projections for each detector over the projection angles, high-pass filtering the averaged projections, and using those offsets as corrections to each detector.

Figure 11(a), shows a partial reconstruction of a third generation scan with detector-to-detector imbalances. Notice the concentric rings in the reconstructed image. The complimentary image Figure 11(b) illustrates the reconstruction of the same data set with the Kowalski algorithm applied. The line-out in Figure 11(c) shows the improved results with the application of the algorithm with no overall magnitude shift in the data.

D) "Tuning-fork" or centering artifacts

In this section, the effects of systematic errors from incorrectly specifying the center of rotation of a scanned object is studied. We begin by presenting experimental data of a two-dimensional circular object (Figure 12). The incorrect specification of the projected rotational center causes the filtered backprojection integral to introduce an artifact that has a "tuning-fork" appearance in the reconstructed image, as well as a distortion of the circular body of the object [AZE90a]. Notice that not only is the tuning-fork effect gone when the center is correct, but the object appears to be circular, as it should be.

This artifact may be minimized by using one of several techniques: (1) an accurate measurement of the center of rotation (sometimes highly impractical); (2) image reconstruction using different centers until the correct one is found (usually very time consuming); or (3) computation of the center of rotation from the sinogram. We perform the latter by an algorithm that essentially consists of: (1) forming a signal of the computed center-of-mass for each projection (over 180 degrees), and (2) fitting a sinusoid of known frequency to the signal; using the sinusoidal offset as an estimate of the center of rotation. For a complete description and analysis of this algorithm see [AZE90a].

IV. CONCLUSIONS

In this work, we examine four geometric effects that are common to first- and third-generation (parallel beam, 180 degree) computerized tomography scanners. The geometric effects focused on in this paper are: X-pattern, edge-generated ringing, circular-ring, and tuning-fork artifacts.

The study conducted on X-pattern artifacts (caused by several possible errors) indicates the importance of correctly calculating the incident intensity. A second, and very important, result is the verification that the image reconstruction algorithm does not produce the X-

pattern artifact, and therefore must be due to some other physical effects or a preprocessing step that forms the line-integrals.

The edge-generated ringing study points out the importance of determining the "best" reconstruction filter based on noise, edge sharpness, and edge ringing. Insight gained from our study on the edge-generated ringing artifact (due to improper choice of the reconstruction filter and cutoff frequency) suggests that the ramp filter should be avoided so that Gibb's phenomenon at sharp edges is minimized. The Butterworth filter of order six reduces the ringing artifact at a cost of slightly smoother edges.

Studies conducted on data with circular-ring artifacts (caused by employing balanced detectors) suggests that gain or offset imbalances from detector to detector in linear- or area-array detector systems produces concentric rings in the reconstructed image. A signal processing technique which minimizes this artifact is given.

The final geometric artifact, the "tuning-fork" artifact in the reconstructed image (generated by an incorrectly specified center-of-rotation), may be minimized by computing the center of rotation from the sinogram. This simple procedure can be done in software.

The underlying theme of the collective studies is that we can achieve improved CT reconstructions by paying careful attention to all sources of potential error in CT scanning systems and the reconstruction codes.

ACKNOWLEDGMENTS

We would like to thank W. Small for helping with the figures and A. E. Pontau for providing us with the PEL data. The authors would also like to acknowledge the Engineering Research program and the Nondestructive Evaluation (NDE) Section at LLNL for supporting this work.

REFERENCES

[ANT89] A. J. Antolak and A. E. Pontau, "Analysis of Polystyrene and Carbon Foam Morphologies Using Proton Beams", *Nucl. Instr. and Meth.* **B40/41**(1989)659.

[AZE88] S. G. Azevedo, A. J. De Groot, D. J. Schneberk, J. M. Brase, H. E. Martz, A. K. Jain, W. Current, and P. Hurst, "Tomographic Image Reconstruction

Using Systolic Array Algorithms", *Review of Progress in Quantitative Nondestructive Evaluation* **8A**(1989)415.

[AZE90] S. G. Azevedo, H. E. Martz, M. F. Skeate, D. J. Schneberk, and G. P. Roberson, "Computed tomography Software and Standards", Lawrence Livermore Laboratory National Laboratory internal report (to be published).

[AZE90a] S. G. Azevedo, D. J. Schneberk, J. P. Fitch, and H. E. Martz, "Calculation of the Rotational Centers in Computed Tomography Sinograms", Lawrence Livermore Laboratory National Laboratory Report UCRL-102615, accepted by *IEEE Trans. Nuc. Sci.* (in press).

[BAR81] H. H. Barrett and W. Swindell, Radiological Imaging: Theory of Image Formation, Detection, and Processing, (Academic Press, New York, 1981) Vol. 1 and 2.

[HER80] G. T. Herman, Image Reconstruction from Projections: The Fundamentals of Computerized Tomography, (Academic Press, New York, 1980).

[JAI89] A. K. Jain, Fundamentals of Digital Image Processing, (Prentice - Hall, Englewood Cliffs, New Jersey, 1989).

[KOW78] G. Kowalski, "Suppression of ring artifacts in CT fan-beam scanners," *IEEE Trans. Nuclear Science*, Vol. NS-25, No. 5, Oct 1978, pp. 1111-1116.

[MAR88] H. E. Martz, S. G. Azevedo, J. M. Brase, K. E. Waltjen, and D. J. Schneberk, "Computed Tomography Systems and Their Industrial Applications", Lawrence Livermore National Laboratory, UCRL 98492, (1988), and accepted by *Appl. Radiat. Isot.* (in press).

[MAR89] H. E. Martz, M. F. Skeate, D. J. Schneberk, and S. G. Azevedo, "Design, Performance, and Application of a CCD Camera-Based CT System", Lawrence Livermore National Laboratory, UCRL 101263, (1989), and *The American Society for Nondestructive Testing Topical Conference on Industrial Computerized Tomography Topical Proceedings* , July 25-27, Seattle, WA, Am. Soc. for NDT, Columbus OH (1989)34.

[MAR90] H. E. Martz, D. J. Schneberk, S. G. Azevedo, and S. K. Lynch, Lawrence Livermore National Laboratory, UCRL 102345, (1989), and submitted to Nondestructive Characterization of Materials **4**, Plenum Publishing Corp., New York, (1990).

[PON89] A. E. Pontau, A. J. Antolak, D. H. Morse, A. A. Ver Berkmoes, J. M. Brase, D. W. Heikkinen, H. E. Martz, and I. D. Proctor, "Ion Microbeam Tomography", *Nucl. Instr. and Meth.* **B40/41**(1989)646.

[RAB75] L. R. Rabiner and B. Gold, Theory and Application of Digital Signal Processing, (Prentice - Hall, Englewood Cliff, New Jersey, 1975).

[SCH89] D. J. Schneberk, H. E. Martz, S. G. Azevedo, and M. F. Skeate, "Data Acquisition Errors and the Choice of Filter in Filtered Backprojection Algorithms" Lawrence Livermore Laboratory National Laboratory, UCRL-101264, (1989), and *The American Society for Nondestructive Testing Topical*

Conference on Industrial Computerized Tomography Topical Proceedings , July 25-27, Seattle, WA, Am. Soc. for NDT, Columbus OH (1989)108.

[SCH90] D. J. Schneberk, S. G. Azevedo, H. E. Martz, and M. F. Skeate, "Sources of Error in Industrial Tomographic Reconstructions", Lawrence Livermore National Laboratory, UCRL-JC-103191, *Mat. Eval.***48**(1990)609.

Figure Captions

Figure 1. PEL tomographic images of a uniform square object. Each image from left to right, top to bottom represents one slice, two adjacent slices summed, three adjacent slices summed, etc. Notice the electron density X pattern in each slice. The object inspected was known to be uniform. Thus we do not believe the X to be due to a density variation within the object, but that it must be caused by some unknown effect(s). (Data courtesy of Art Pontau and Dan Morse of Sandia National Laboratory, Livermore.)

Figure 2. Reconstructed images simulating a negative incident intensity bias for projection data of a uniform simulated square. (a) The original object consists of a 64 by 64 pixel image with an included 32 by 32 square of unit attenuation. The projections of this object were simulated, reduced by 50%, 30%, and 10% of their maximum value, and reconstructed (shown in (b), (c) and (d) respectively). Horizontal (from left to right at the center) and diagonal (upper left to middle) line-outs of the various reconstructions are displayed in (e) and (f) respectively.

Figure 3. Reconstructed images simulating a positive incident intensity bias for simulated projection data of the uniform square. (a) The original object is the same as in Figure 2(a), but is shown here at the appropriate intensity scale for this problem (since the projections are larger, due to the positive bias being added). The projections of this object were simulated, increased by 50%, 30%, and 10% of their maximum value, and reconstructed (shown in (b), (c) and (d) respectively). Horizontal (from left to right at the center) and diagonal (upper left to middle) line-outs of the various reconstructions are displayed in (e) and (f) respectively.

Figure 4. Edge-ringing caused by the ramp filter with different cutoff frequencies. Actual dat is shown reconstructed using filter cutoffs of (a) 0.15, (b) 0.25, and (c) 0.35 times the fold-over frequency. Notice the appearance of ringing illustrated in the line-outs (d) that changes with cutoff frequency. The reconstructed object is PBX9502 which is a very uniform high explosive material. The projection data was acquired using PBCAT [MAR90], a first-generation scanner.

Figure 5. Ramp filter study results for a simulated circular object. (a) The original object consists of a 64 by 64 image with a circle at the center of rotation with unit attenuation. The projections of this object were simulated, and then reconstructed using a ramp filter in the FBP algorithm at cutoffs of (b) 0.1, (c) 0.3, and (d) 0.5 times the fold-over frequency.

Figure 6. Butterworth filter study results for a simulated circular object. The original object is the one shown in Figure 5(a). The projections of this object were simulated, and then reconstructed using a sixth-order Butterworth filter in the FBP algorithm at cutoffs of (b) 0.1, (c) 0.3, and (d) 0.5 times the fold-over frequency.

Figure 7. Horizontal line-outs through the center of the ramp and Butterworth filtered images shown in Figures 5 and 6.

Figure 8. Ramp filter study results for a simulated square object. (a) The original object consists of a 64 by 64 image with an included 32 by 32 square at the center of rotation with unit attenuation . The projections of this object were simulated, and then reconstructed using a ramp filter in the FBP algorithm at cutoffs of (b) 0.1, (c) 0.3, and (d) 0.5 times the fold-over frequency.

Figure 9. Butterworth filter study results for a simulated square object. The original object is the one shown in Figure 8(a). The projections of this object were simulated, and then reconstructed using a sixth-order Butterworth filter in the FBP algorithm at cutoffs of (b) 0.1, (c) 0.3, and (d) 0.5 times the fold-over frequency.

Figure 10. Horizontal line-outs through the center of the ramp and Butterworth filtered images of Figures 8 and 9.

Figure 11. Circular ring artifacts caused by detector-to-detector imbalances in a third generation scan. (a) The reconstructed image with the imbalanced projections produces a noticeable concentric ring pattern. (b) A reconstructed image of the same data set after applying the Kowalski algorithm reduces the artifact effectively. (c) The line-outs through the high-density inclusion show some smoothing of the noise with little distortion of the true features.

Figure 12. Artifacts due to an incorrect specification of the center-of-rotation. The correct projection center is a value of 140 (shown in (c)) whose reconstruction shows no artifacts. Other reconstructions with incorrect centers ((a), (b), (d), and (e)) display a distorted object and the "tuning-fork" artifact.

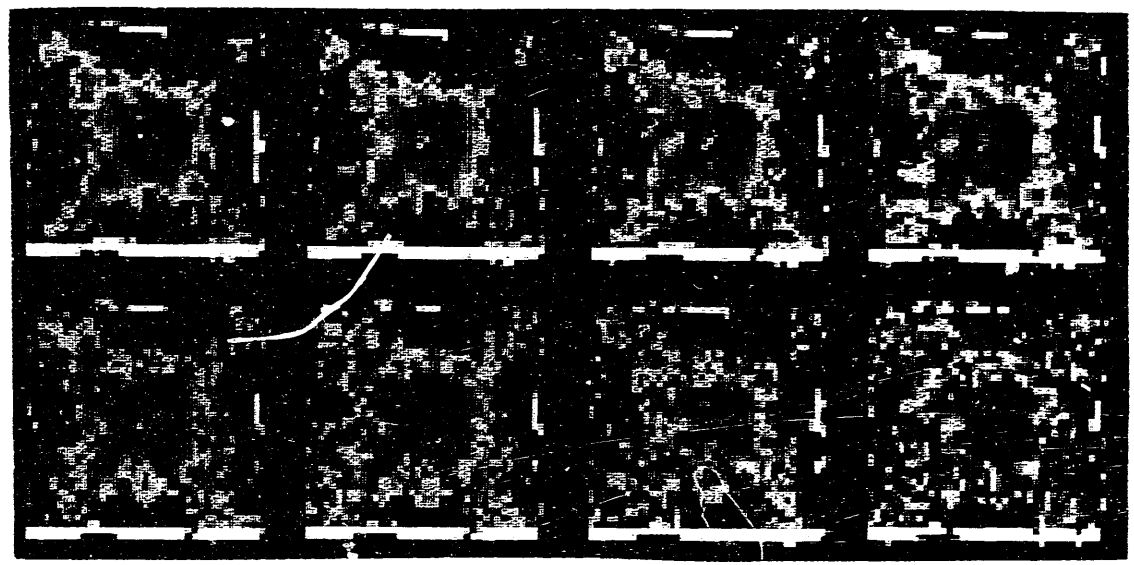

Figure 1. PEL tomographic images of a uniform object.

These data simulate a negative bias added to the projections

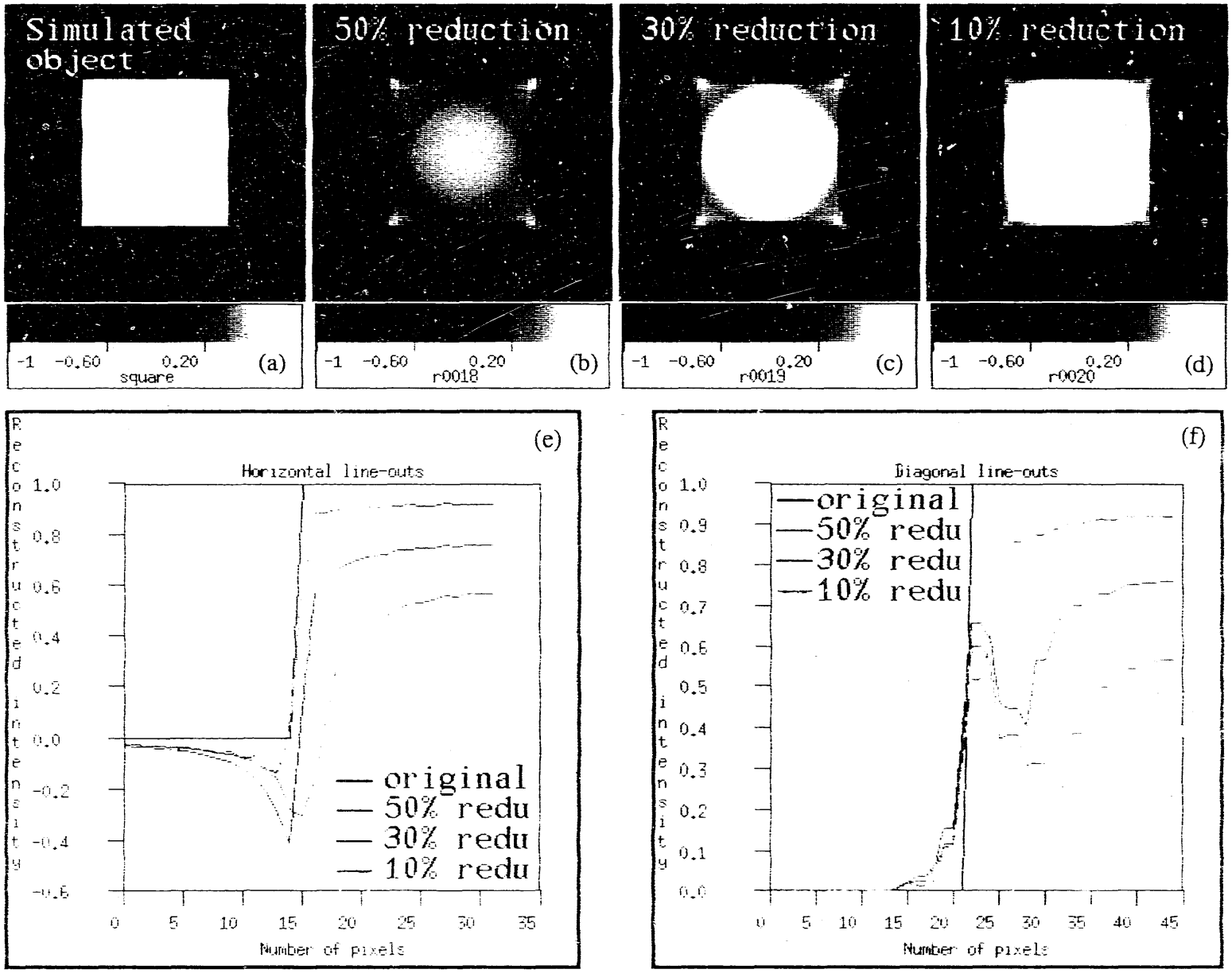

Figure 2.

These data simulate a positive bias added to the projections

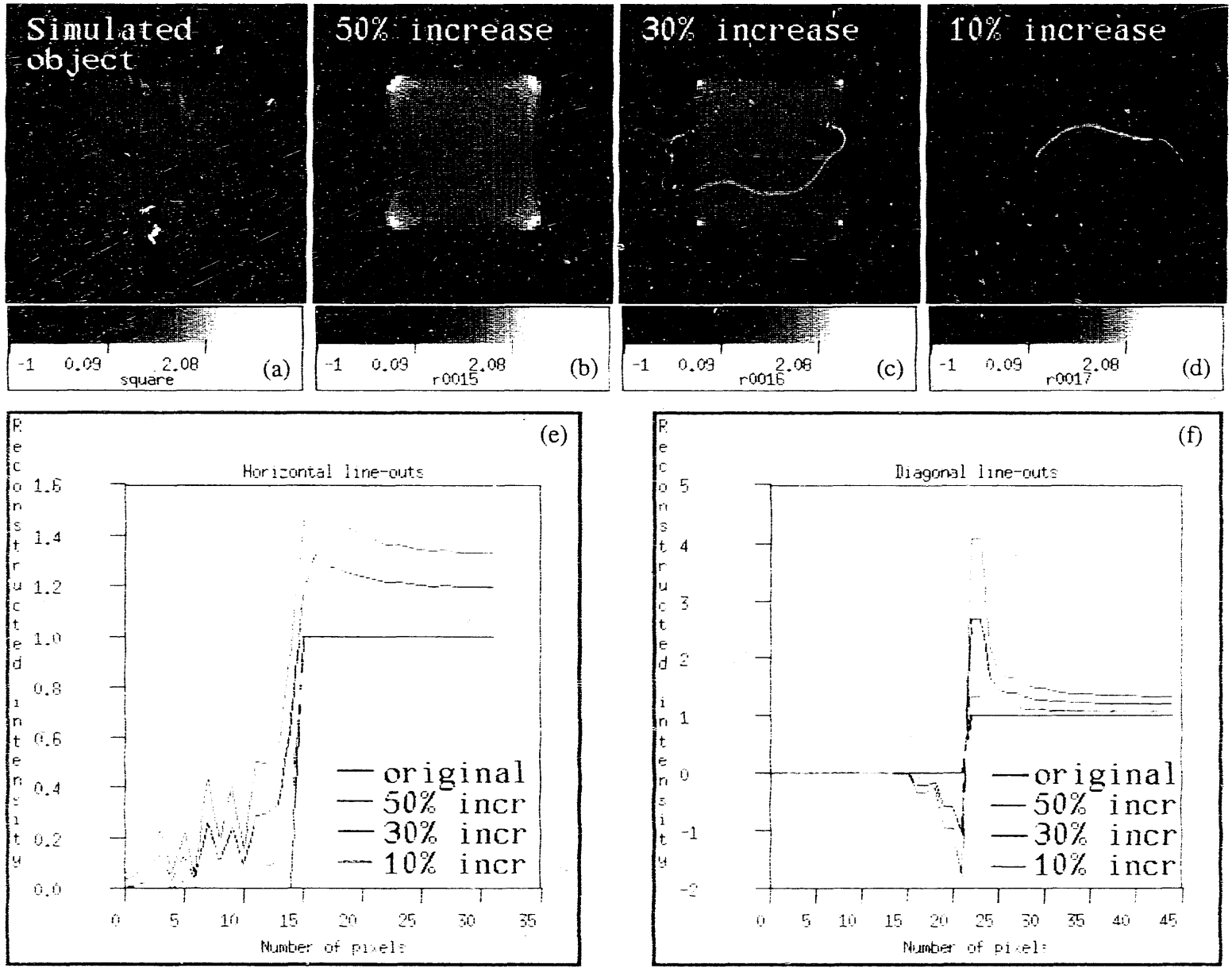

Figure 3.

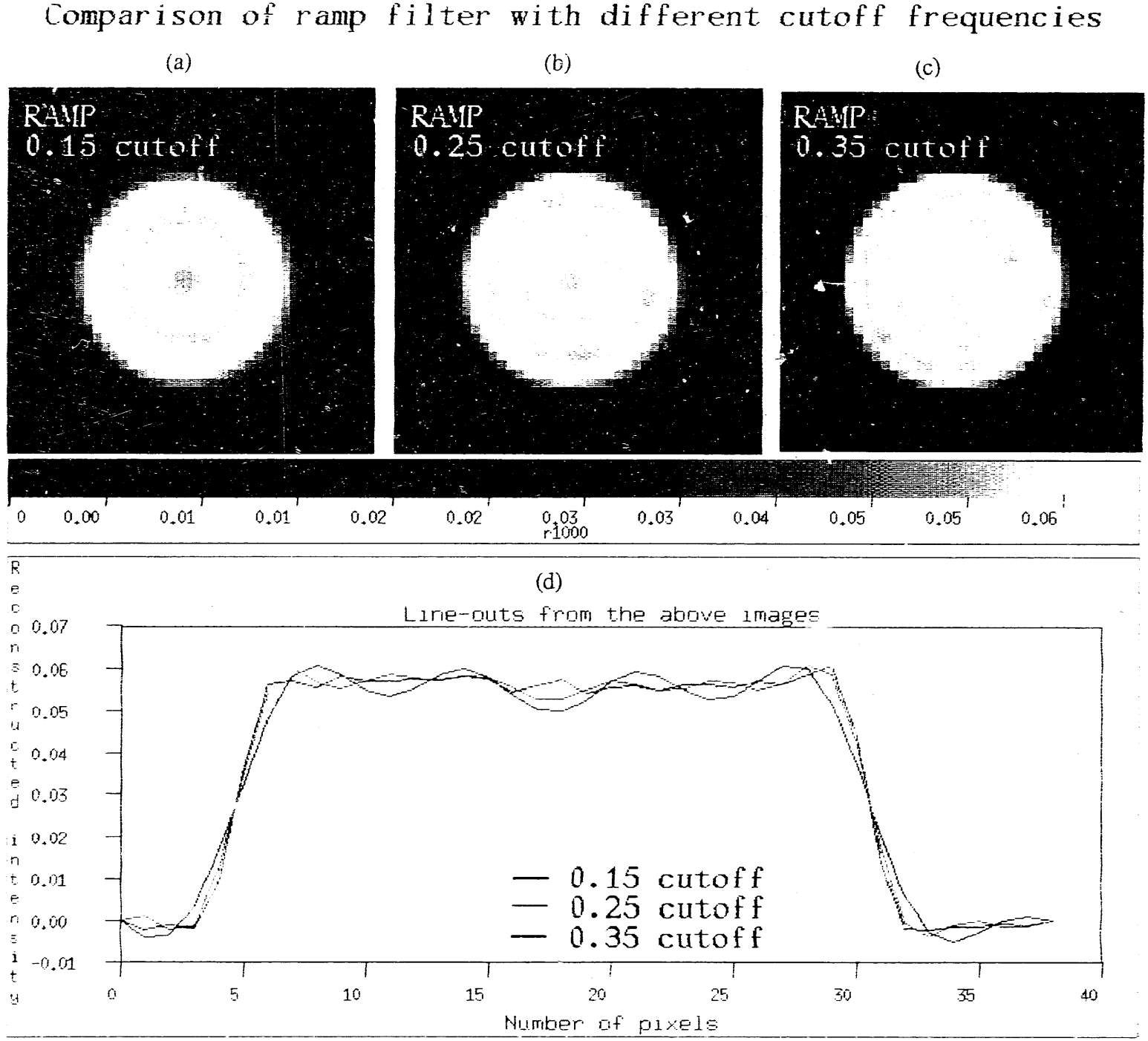
Comparison of ramp filter with different cutoff frequencies
(a)
(b)
(c)
RAMP
0.15 cutoff
RAMP
0.25 cutoff
RAMP
0.35 cutoff
0
0.00
0.01
0.01
0.02
0.02
0.03
0.03
0.04
0.05
0.05
0.06
r-1000
(d)
Line-outs from the above images
Reconstructed intensity
0.07
0.06
0.05
0.04
0.03
0.02
0.01
0.00
-0.01
0
5
10
15
20
25
30
35
40
Number of pixels
0.15 cutoff
0.25 cutoff
0.35 cutoff

Figure 4.

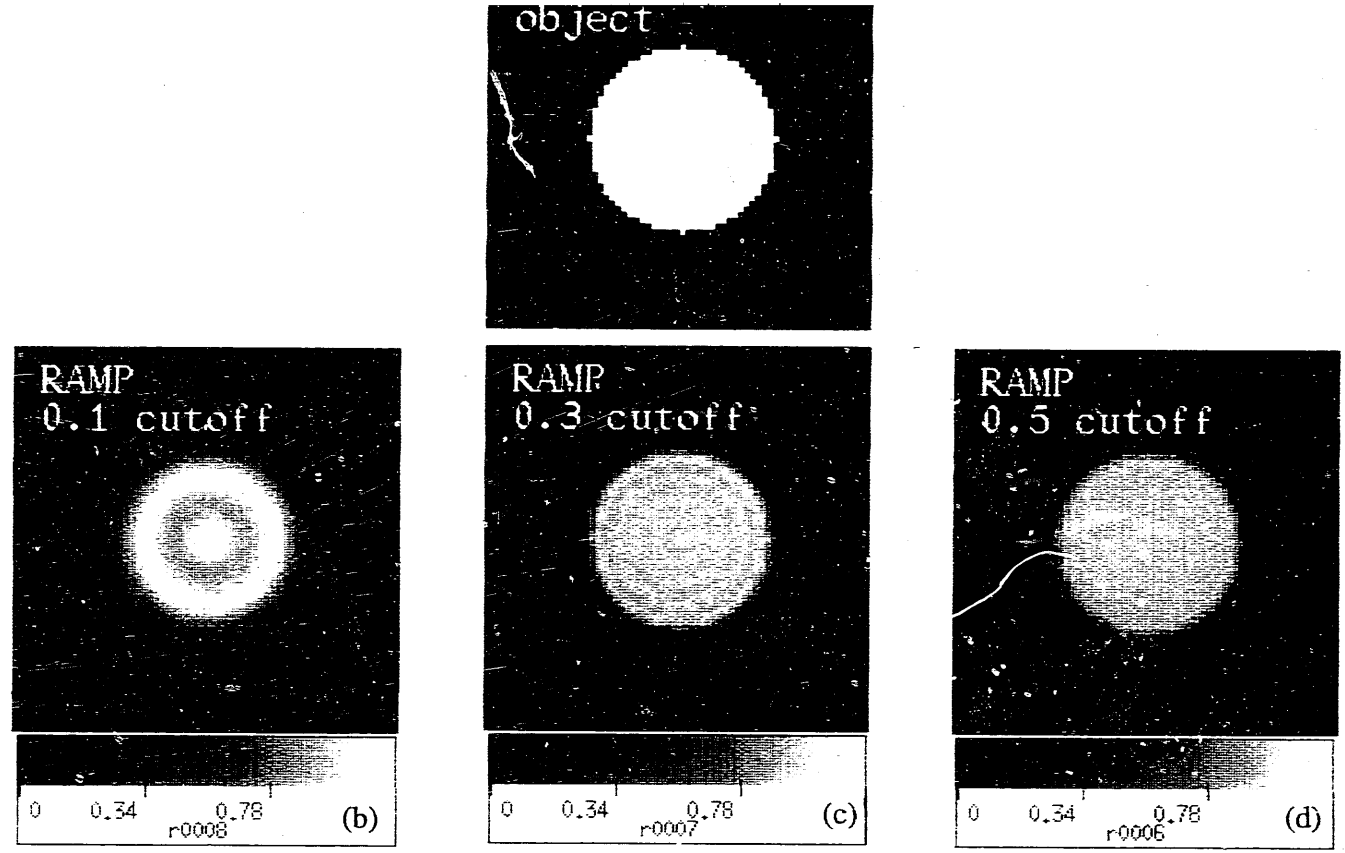

Figure 5. Ramp filter study results for a simulated circular object

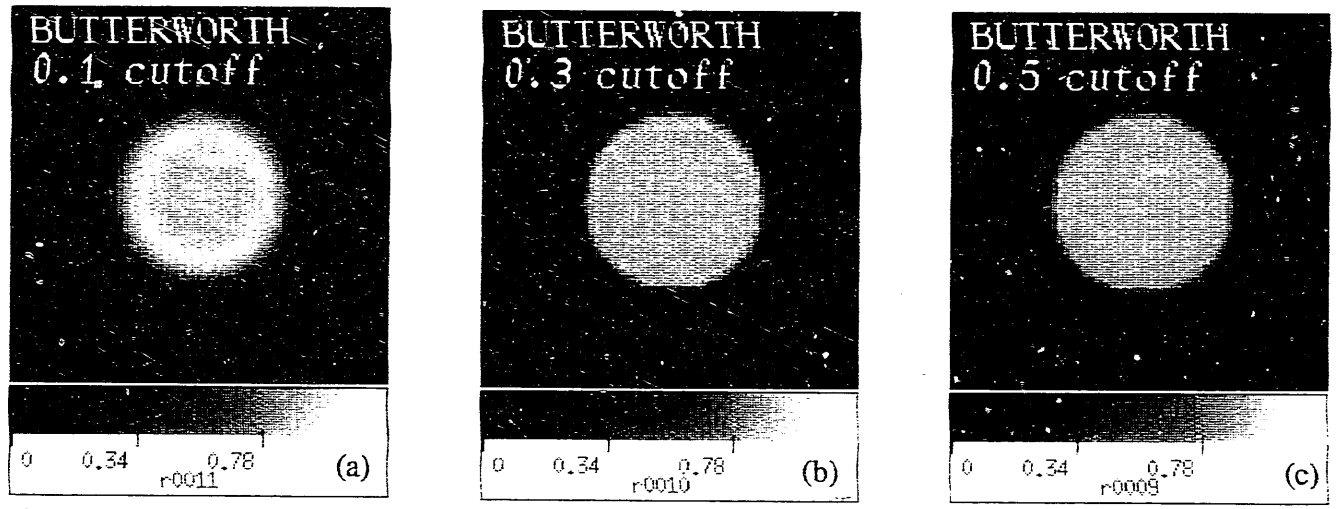

Figure 6. Butterworth filter study results for the circular object

Line-outs from the ramp and Butterworth filtered reconstructions

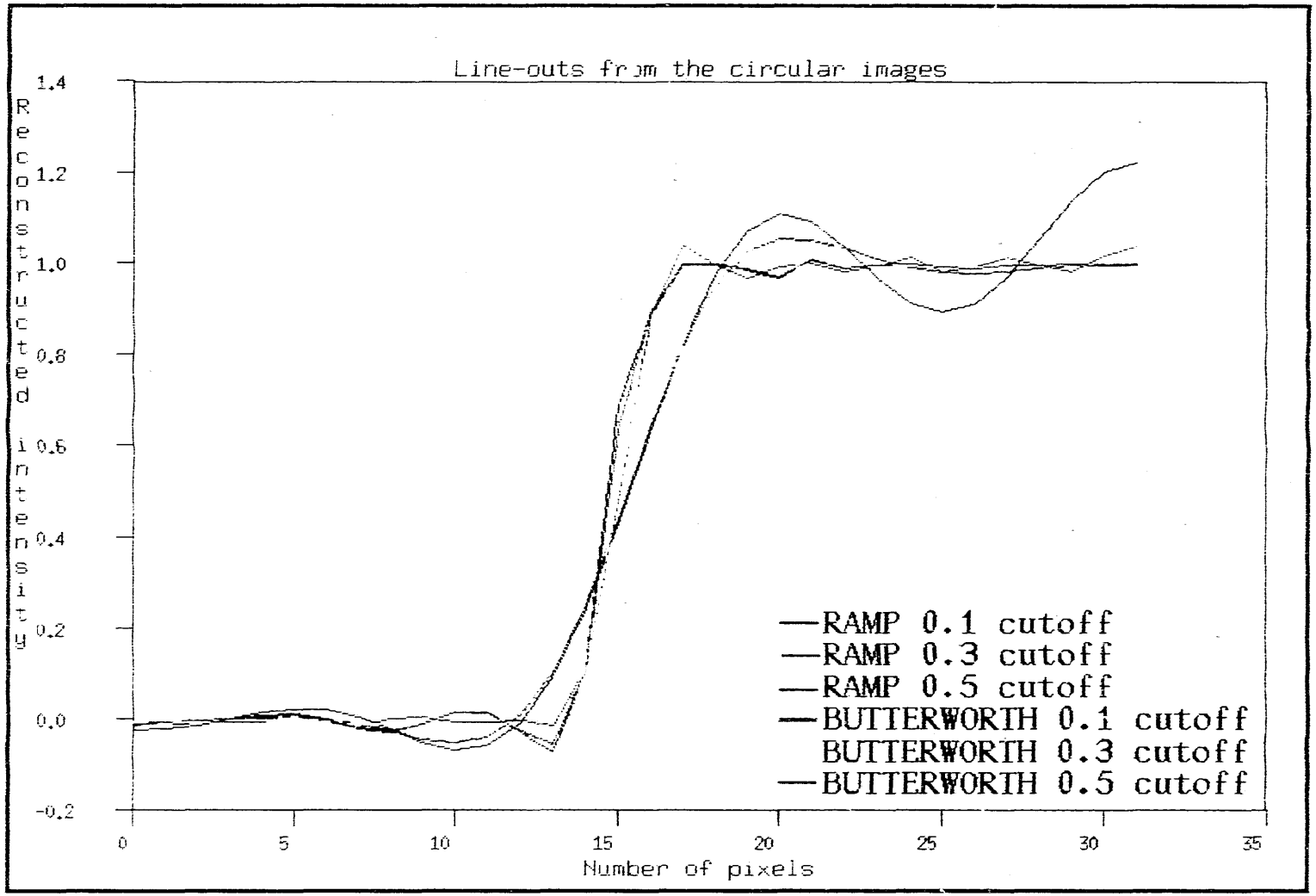

Figure 7.

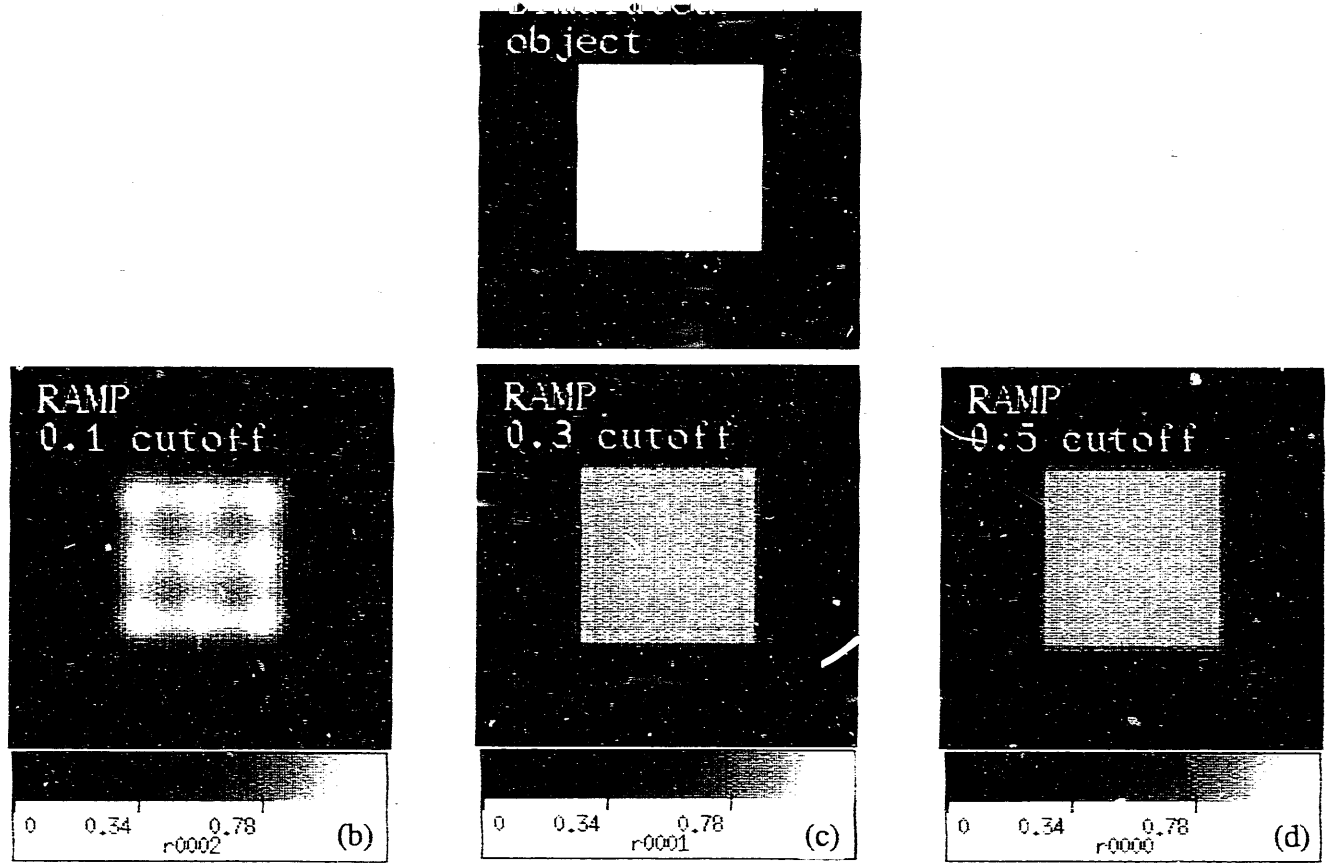

Figure 8. Ramp filter study results for a simulated square object

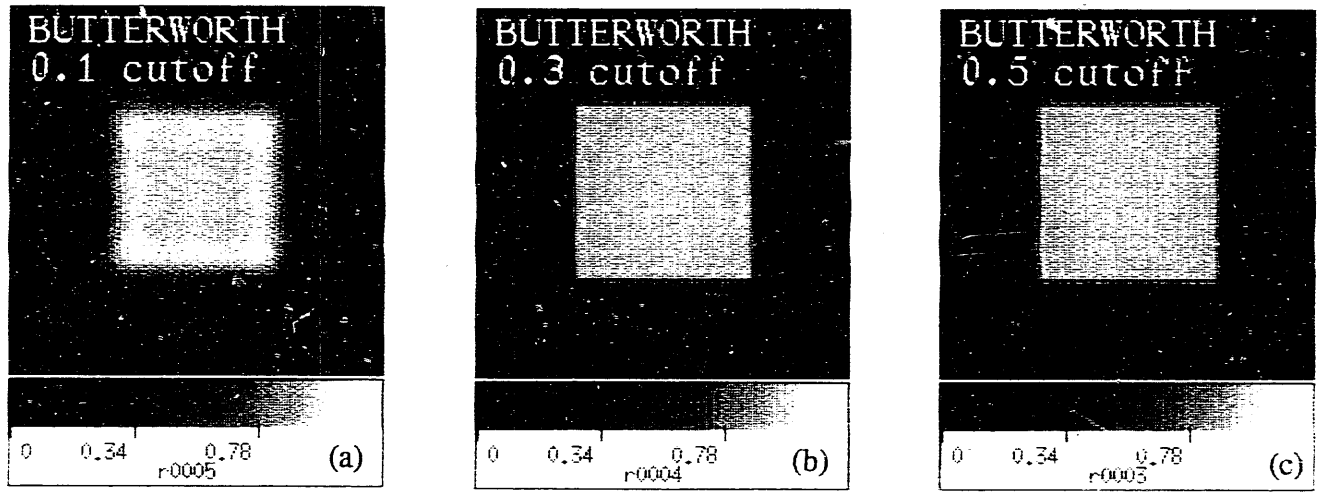

Figure 9. Butterworth filter study results for the square object

Line-outs from the ramp and Butterworth filtered reconstructions

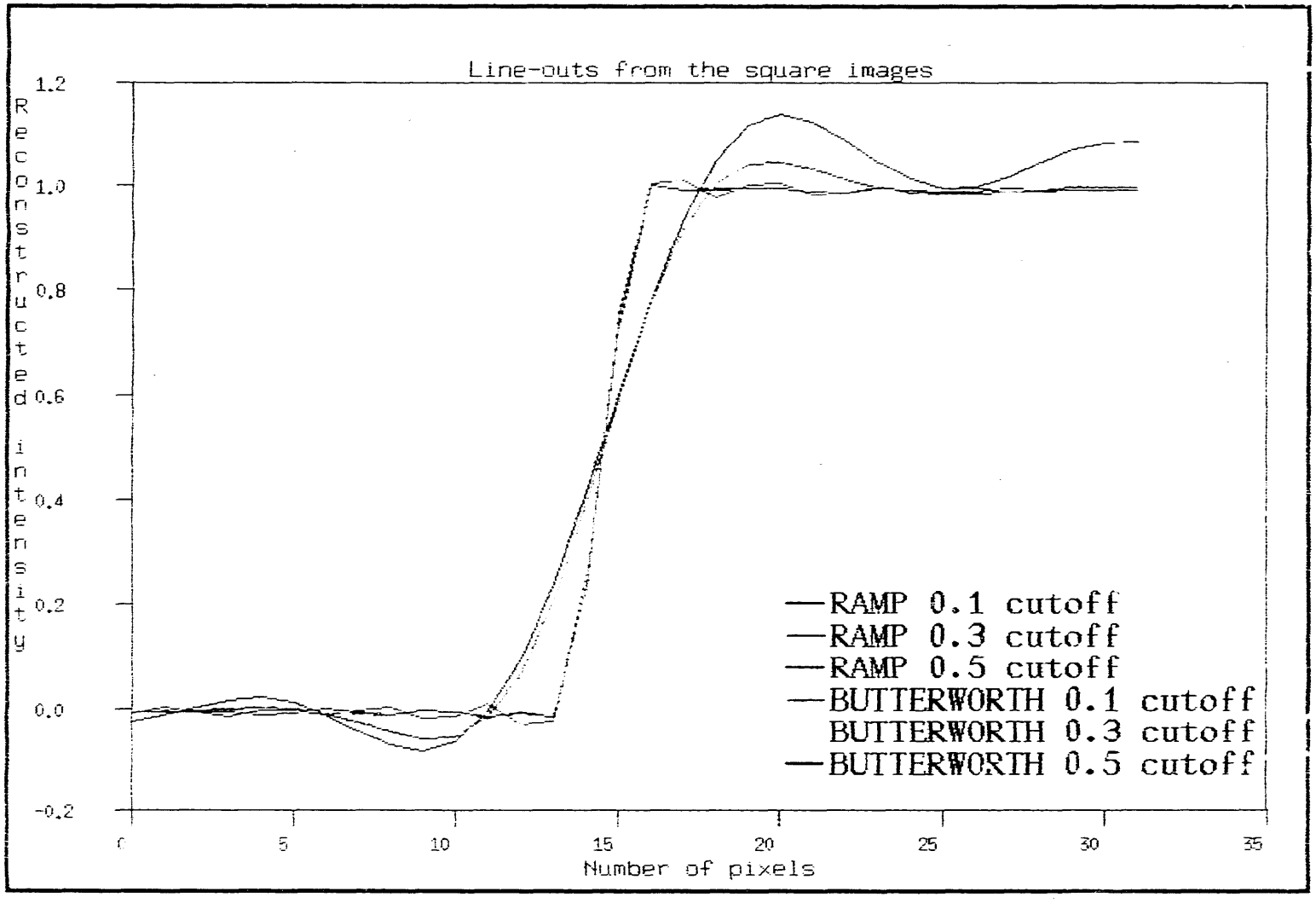

Figure 10.

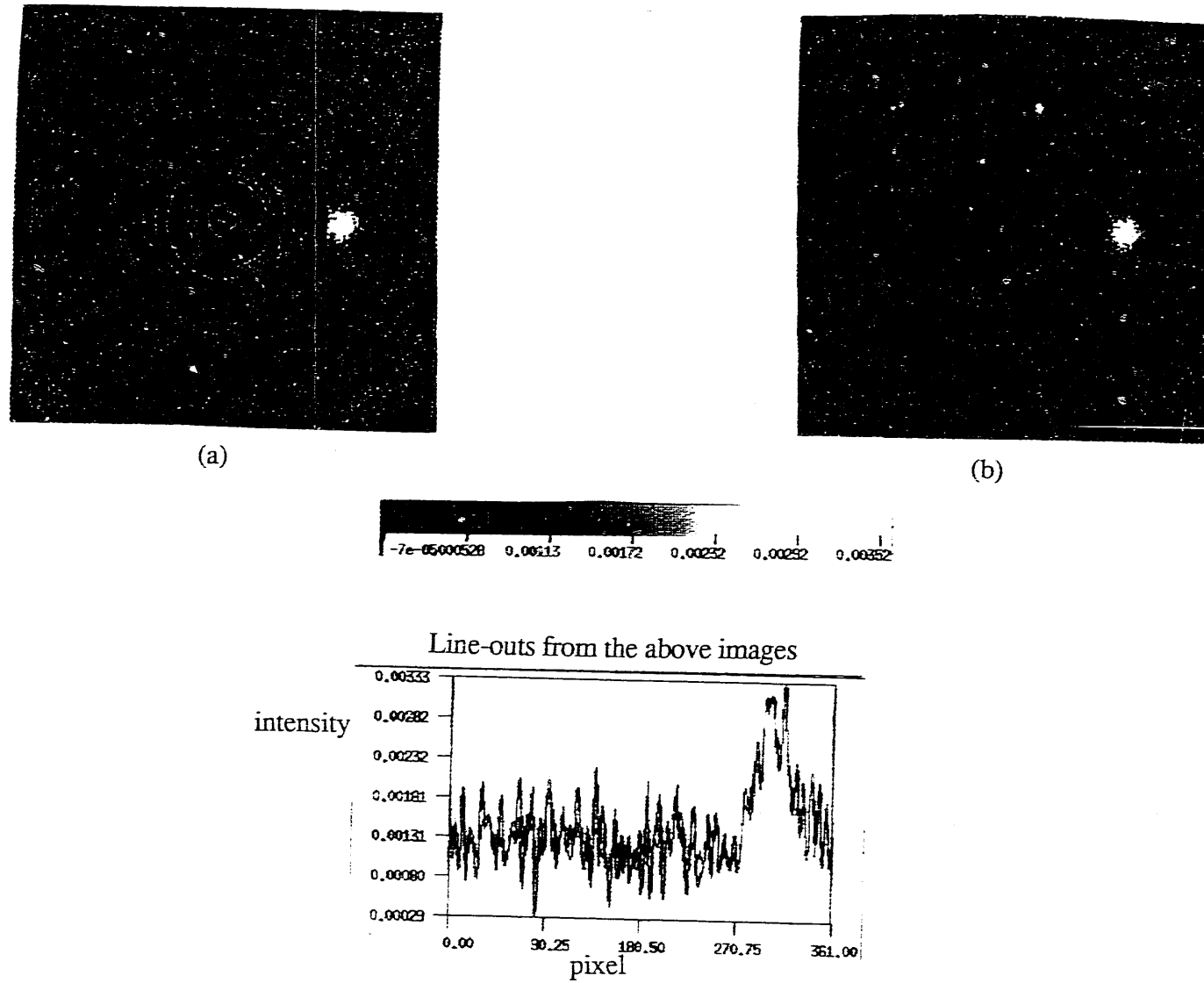

Figure 11. Reconstruction of a third generation scan with detector-to-detector imbalances.

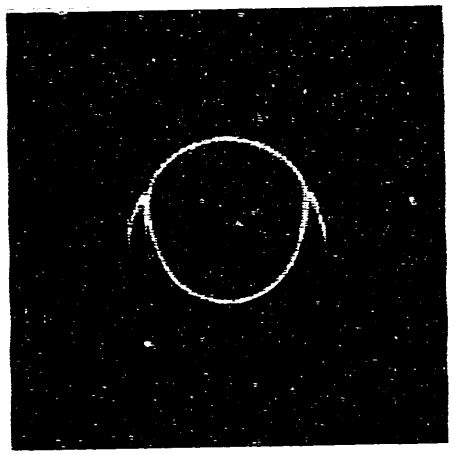

center = 134

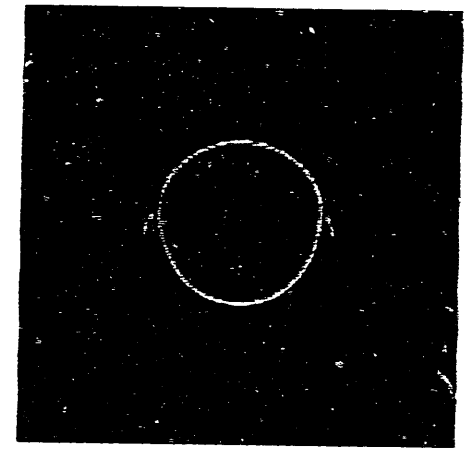

center = 137

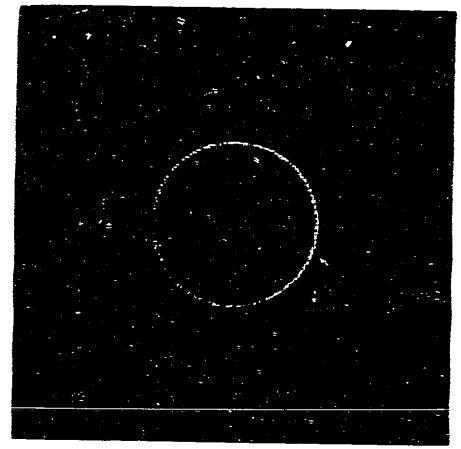

center = 140 (correct)

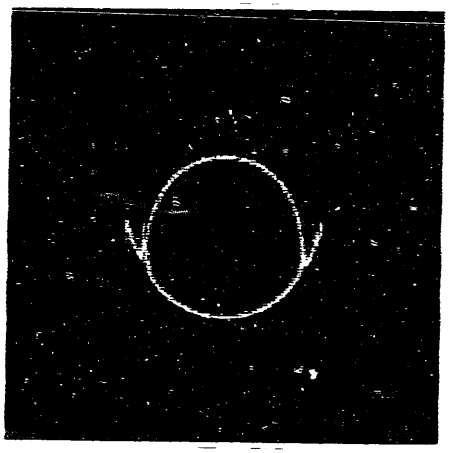

center = 147

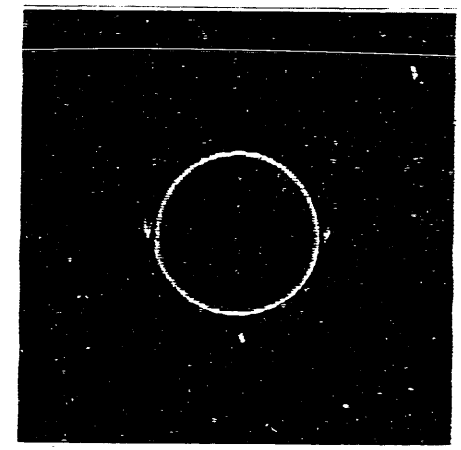

center = 143

Figure 12. Artifacts due to an incorrect specification of the center-of-rotation.

END

DATE FILMED

12/10/90